Journal of Applied Fluid Mechanics, Vol. 18, No. 9, pp. 2239-2251, 2025.
Available online at www.jafmonline.net, ISSN 1735-3572, EISSN 1735-3645.
https://doi.org/10.47176/jafm.18.9.3392

Numerical Simulation of Hydrodynamic Forces on an Underwater Vehicle Near the Free Surface

M. S. Ahmad[1,2], M. A. A. Hasnan[1,2†], N. M. R. Shaharuddin[1,2], M. N. A. W. Muhammad Yazid[1], I. Shah[3] and M. Mohsin[1]

[1] *Faculty of Mechanical Engineering, Universiti Teknologi Malaysia, Skudai, Johor,81310, Malaysia*
[2] *Marine Technology Centre, Faculty of Mechanical Engineering, Universiti Teknologi Malaysia, Skudai, Johor, 81310, Malaysia*
[3] *Department of Mechatronics Engineering, Air University, Islamabad 44000, Pakistan*

†*Corresponding Author Email: muhammedamirulasyraf@utm.my*

ABSTRACT

Underwater Vehicles (UVs), including Autonomous and Remotely Operated Vehicles, are increasingly utilized in marine applications such as exploration, surveying, and defense. The hydrodynamic performance of UVs, particularly their resistance and lift characteristics near the free surface, plays a crucial role in their design and operational efficiency. This research employs Computational Fluid Dynamics (CFD) simulations to analyze the behavior of an underwater vehicle operating at various depths near the free surface. Two configurations of the DARPA SUBOFF model: the bare hull (AFF-1) and the fully appended configuration (AFF-8) were investigated. Simulations were conducted under different operating conditions, and numerical results were validated against experimental and existing numerical data to ensure accuracy and reliability. The interaction between the underwater vehicle and the free surface is analyzed to understand its effects on hydrodynamic performance. The findings demonstrate a significant impact of the free surface on resistance and lift, with the appendages in the AFF-8 configuration leading to more pronounced hydrodynamic effects, particularly at higher speeds where wave generation and interaction with the free surface are increased. These results highlight the effects of speed, depth, and vehicle configuration on hydrodynamic performance, providing valuable insights for the design and optimization of UVs. This study serves as a valuable foundation for further exploration of operational strategies and the development of UVs across diverse marine applications.

Article History

Received January 20, 2025
Revised April 14, 2025
Accepted April 16, 2025
Available online July 5, 2025

Keywords:

Underwater vehicles
Free surface interaction
DARPA suboff
Hydrodynamics
Computational fluid dynamics

1. INTRODUCTION

Underwater vehicles play a crucial role in a wide range of industries, including marine research, defense, oil and gas exploration, and underwater infrastructure inspection. These vehicles, which include remotely operated vehicles (ROVs) and autonomous underwater vehicles (AUVs), are designed to perform complex tasks in deep and shallow waters, often in environments that are otherwise inaccessible to humans. Their capabilities are vital for underwater mapping, environmental monitoring, search and rescue missions, and scientific exploration of the deep sea. Near the free surface or at shallow depths, these vehicles are particularly useful in coastal surveys, pipeline inspections, and offshore structure maintenance, where precise maneuverability is required. However, operating near the surface presents unique challenges, as hydrodynamic forces such as resistance and lift become more complex and unpredictable. When an underwater vehicle operates near the free surface, it experiences increased hydrodynamic resistance and lift. These effects arise from the interaction with the free surface, which introduces wave resistance. This phenomenon is usually absent in deeply submerged conditions (Ahmad et al., 2024). As the submergence depth increases, the influence of the free surface diminishes, leading to a reduction in these hydrodynamic effects (Lambert et al., 2023; Luo et al., 2023). The wave resistance encountered by underwater vehicles is significantly influenced by the Froude number; as the vehicle approaches the free surface, resistance coefficients increase, underscoring the substantial impact of the free surface on overall hydrodynamic performance (Mitra et al., 2020).

Recent advancements in the hydrodynamics of underwater vehicles maneuvering near the free surface

Nomenclature

C_T	total resistance coefficient	D	maximum diameter of the vehicle
C_L	total lift coefficient	F_i	body force component in each direction
F_r	Froude number	k	turbulence kinetic energy
μ	dynamic viscosity	ω	specific dissipation rate in turbulence model
GCI	Grid Convergence Index	L_{PP}	length between perpendiculars
L_{OA}	overall length of the vehicle	R_G	grid convergence condition
V	velocity of the vehicle	ρ	fluid density
ν	kinematic viscosity	g	gravitational acceleration

have significantly enhanced our understanding of their dynamics through innovative modelling techniques and experimental validations. Battista et al. (2023) developed a nonlinear, time-dependent parametric motion model incorporating free surface effects using energy-based modelling techniques. This approach accounts for instantaneous energy stored in the free surface and fluid memory effects. By employing the Euler–Lagrange equations, researchers have derived six-degree-of-freedom (6DOF) nonlinear equations of motion that accurately reflect these dynamics. Valentinis et al. (2023) extended this model to include ambient wave effects and demonstrated its application in a nonlinear depth-keeping control system Lambert et al. (2023) combined a lumped parameter maneuvering model with free surface corrections, using CFD simulations and frequency domain strip theory to account for added mass changes, memory forces, and wave excitation forces. These models significantly enhance our understanding of underwater vehicle dynamics near the free surface, particularly in terms of maneuverability and stability under various conditions. Besides studies on flow characteristics, scour reduction, discharge coefficients, and energy loss prediction in hydraulic structures provide valuable insights into fluid behavior and modeling approaches (Abbaszadeh et al., 2023a, b; Daneshfaraz et al., 2023; Abbaszadeh et al., 2024).

The calculation of hydrodynamic coefficients is essential for understanding the maneuverability of underwater vehicles. Various methodologies have been employed to estimate these coefficients, including theoretical estimations, system identification based on actual navigation data, and numerical simulations using tools like FLUENT, StarCCM etc. Each method presents unique advantages and limitations, highlighting the complexity of accurately modelling underwater dynamics (Mitra et al., 2019; Ilyas et al., 2023; Jiawei et al., 2023). Recent studies have also emphasized the importance of considering environmental factors, such as wave interactions and surface proximity, which can significantly influence the hydrodynamic performance of these vehicles (Walker et al., 2021). Moreover, the hydrodynamic performance of bio-inspired designs, such as fish-like robots operating near the surface, has been investigated. Research indicates that parameters like attack angles, oscillating amplitude, and environmental conditions play a critical role in determining thrust and vertical forces generated by these vehicles (Xu et al., 2024b). The Virginia Tech team has contributed to this field by developing a lumped parameter maneuvering model (LPM) that effectively predicts the maneuvering motions of deeply submerged vehicles while accounting for free surface effects. Their findings demonstrate that identical maneuvering inputs yield different motion histories when vehicles are near the surface compared to deeper water scenarios (Meng et al., 2022).

Simulation methods for shallowly submerged vehicles have also been explored, revealing significant differences in hydrodynamic responses when comparing linearized free surface boundary conditions to more complex models. These studies indicate that at small submergences and high velocities, the hydrodynamic responses can vary dramatically, necessitating careful consideration in the design and control of underwater vehicles (F-Pedrera Balsells et al., 2020). The DARPA SUBOFF submarine hull form has been a focal point of research, illustrating that free surface effects diminish rapidly with increased submergence and are highly dependent on the Froude number, which is critical for understanding vehicle performance in varying operational conditions (Ling et al., 2022). Incorporating free-surface and ambient wave effects into nonlinear parametric models has been shown to enhance the performance of depth-keeping control systems for submarines, effectively compensating for parasitic hydrodynamic effects during maneuvers (Gabriel et al., 2020).

The hydrodynamics of underwater vehicles (UVs) operating near the free surface remains an area of active research, yet significant gaps persist in understanding the complex interactions that occur in this regime (Xu et al., 2024a). While existing studies have explored various aspects of underwater vehicle dynamics, including hydrodynamic coefficients and maneuverability, there is a lack of comprehensive numerical simulations that specifically address the effects of free surface proximity on drag and lift for both bare and fully appended hull configurations of DARPA SUBOFF. Most current research focuses on either model tests or theoretical approaches, which often do not capture the intricate fluid dynamics involved when Underwater vehicles operate at varying depths and speeds near the free surface. The existing literature also tends to concentrate on specific vehicle types or configurations without appendages, leaving a gap in understanding how different hull designs, such as the DARPA SUBOFF bare hull and fully appended hull, respond to free surface effects under various operational conditions (Zhang et al., 2024). Additionally, the impact of turbulence on hydrodynamic forces has not been extensively studied about Underwater vehicles near the free surface.

The primary objective of this study is to conduct a detailed numerical simulation of the hydrodynamic performance of the DARPA SUBOFF bare hull and fully appended hull configurations using ANSYS Fluent. Unlike previous studies that primarily focus on deeply submerged conditions, this research systematically examines the influence of submergence depth, speed, and appendages on hydrodynamic performance near the free surface. By employing the *k-ω* SST turbulence model in conjunction with the VOF model, the study seeks to accurately capture the complexities of fluid interactions near the free surface, including wave formation and turbulence effects. The novel contribution of this research lies in its comprehensive assessment of near-surface hydrodynamics, quantifying changes in resistance and lift for different hull configurations and operational parameters. Ultimately, this study aims to contribute to the design and operational strategies of underwater vehicles, ensuring improved performance in real-world applications, such as underwater exploration, military operations, and environmental monitoring.

2. NUMERICAL METHODS

2.1 Governing Equations

Numerical simulation is performed using ANSYS Fluent software, which is based on incompressible RANS equations. The RANS equation governs the principle of mass and can be written as:

$$\frac{\partial y}{\partial x_i}(\rho u_i) = 0 \tag{1}$$

Where ρ is fluid density and u_i is the velocity component in each of the directions (*x, y, z*). Equations for conservation of momentum in each direction can be written as:

$$\frac{\partial(\rho u_i)}{\partial t} + \rho u_j \frac{\partial u_i}{\partial x_j} = \rho F_i - \frac{\partial P}{\partial x_i} + \frac{\partial}{\partial x_j}\left[\mu \frac{\partial u_i}{\partial x_j} - \rho \overline{u_i' u_j'}\right] \tag{2}$$

Where F_i is the body force, u_i is time-averaged velocity components in cartesian coordinates x_i (i=1,2,3), P is the time-averaged pressure, μ is the dynamic viscosity, and $\rho\overline{u_i' u_j'}$ is the Reynolds stress tensor.

The finite volume method is employed to discretize the governing eq with the second-order upwind scheme. The Semi-Implicit Method for the Pressure-Linked Equations (SIMPLE) is used for pressure-velocity coupling. To allow the closure of the time-averaged Navier-Stokes equations, various turbulence models were introduced to provide an estimation of the stress tensor. In the current study, the *k-ω* SST turbulence model (Menter, 1994) is used. One of the primary advantages is its ability to accurately predict flow separation and transition from laminar to turbulent flow, which is crucial for analyzing resistance and maneuvering characteristics. The model combines the strengths of the *k-ω* model in the near-wall region with the *k-ε* model in the free stream, enhancing its versatility and robustness across a range of flow conditions. Additionally, the *k-ω* SST model provides improved performance for complex flows with adverse pressure gradients and vortex shedding. The transport equation for turbulence kinetic energy k is given by:

$$\frac{\partial}{\partial t}(\rho k) + \frac{\partial}{\partial x_i}(\rho k u_i) = \partial x_j \partial(\Gamma_k \frac{\partial k}{\partial x_j}) + G_k - Y_k \tag{3}$$

Similarly, the equation for the specific dissipation rate ω is given below:

$$\frac{\partial}{\partial t}(\rho \omega) + \frac{\partial}{\partial xi}(\rho \omega u_i) = \frac{\partial}{\partial x_j}(\Gamma_\omega \frac{\partial \omega}{\partial x_j}) + G_\omega - Y_\omega + D_\omega \tag{4}$$

Where ρ is the fluid density, k is the turbulence kinetic energy, Γ_k and Γ_w is the effective diffusivity of k and ω, G_k and G_w is the production of turbulence kinetic energy due to mean velocity gradients, Y_k and Y_w are the dissipation of k and ω, and D_ω represents the cross-diffusion term that arises in the SST model, which accounts for the combination between the *k-ω* model near the wall and the k-ε model away from the wall. It ensures that the SST model retains the advantages of both models. The density of the fluid, i.e. freshwater, is 998.2 kg/m^3 and dynamic viscosity is 0.001003 Pa-s.

2.2 Volume of Fluid Method

The development of the free surface is captured using the Volume of Fluid (VOF) method, which is widely employed for simulating two-phase flows. The VOF multiphase model belongs to a class of interface-capturing techniques that predict the motion and distribution of immiscible phase interfaces. It has proven effective in modeling free surface flows involving significant deformation and wave motion, as demonstrated by (Chen et al., 2024), highlighting its robustness in multiphase applications. This approach assumes that the mesh resolution is sufficiently fine to resolve the position and shape of the interface accurately. The phase volume fraction and the field α_i describe the phase distribution and the interface location, respectively. The volume fraction of phase i is defined as:

$$\alpha_i = \frac{V_i}{V} \tag{5}$$

Where V is the cell volume, and V_i is the volume of phase i within the cell. The volume fractions of all phases sum to a maximum value of 1, as expressed in Equation 6:

$$\sum_{i=1}^{N} \alpha_i = 1 \tag{6}$$

Where N is the total number of phases. The presence of different phases within a cell is determined by the value of the volume fraction:

- $\alpha_i = 0$ phase i is entirely absent
- $\alpha_i = 1$ the cell is fully occupied by phase i
- $0 < \alpha_i < 1$ indicates the presence of a phase interface

The physical properties of the component fluids are considered when calculating the material properties of the cells at the interface. In cells containing multiple

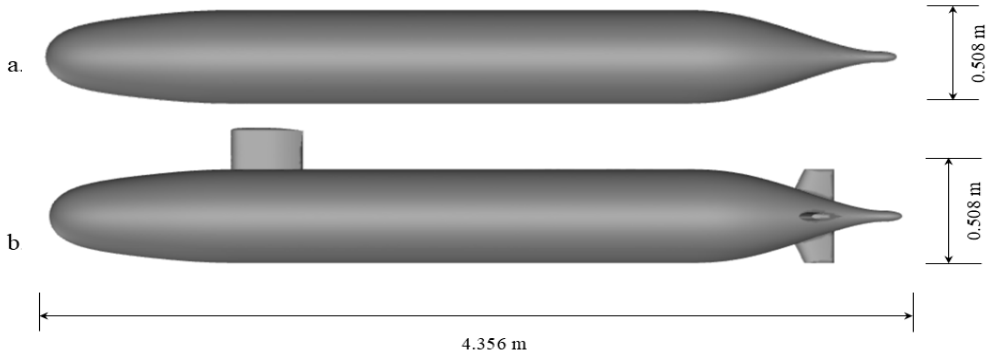

Fig. 1 SUBOFF Geometry (a) AFF-1, (b) AFF-8

Table 1 Dimensions of the SUBOFF Geometry

Parameters	AFF-1	AFF-8
Overall Length (m)	4.356	4.356
Maximum Diameter (m)	0.508	0.508
Centre of Buoyancy L_{CB} (m)	0.4621 L_{OA}	0.4621 L_{OA}
Length between Perpendiculars L_{PP} (m)	4.261	4.261
Volume (m^3)	0.6992	0.706
Wetted surface area (m^2)	5.988	6.350

interfaces, all fluids are treated as part of a single mixture, as shown in Equations 7 and 8.

$$\rho = \sum_i \rho_i \alpha_i \tag{7}$$

$$\mu = \sum_i \mu_i \alpha_i \tag{8}$$

Where ρ_i and μ_i are the density and dynamic viscosity of the phase i, respectively.

2.3 Computational Setup and Geometry

The computational study was conducted using ANSYS Fluent, a robust computational fluid dynamics (CFD) software. The geometries of the AFF-1 and AFF-8 models were generated based on the DARPA SUBOFF specifications given by DTRC (Roddy, 1990). The bare hull (AFF-1) represents a streamlined hull without additional appendages, while the fully appended model (AFF-8) includes external components such as the sail and four stern hydroplanes. These geometries were imported into the GAMBIT meshing tool for further processing. The simulations aimed to investigate the hydrodynamic characteristics, specifically the resistance and lift of these configurations when operating near the free surface. The velocity ranges from $0.153<F_r<0.512$, where F_r refers to the Froude number and is defined by Equation 9:

$$Fr = \frac{V}{\sqrt{gL}} \tag{9}$$

Where V is the velocity of SUBOFF, and g is the gravitational acceleration. The dimensions of the SUBOFF model and 3D view of the SUBOFF bare hull and fully appended models are illustrated in Table 1 and Fig. 1, respectively.

The computational domain was set up following ITTC (2014) recommendations to simulate the Suboff operating near the free surface. The domain extended 2L forward and 5L aft of the model, with 3L below, and 2L above and to the sides (port and starboard), where L is the length overall (LOA) of the Suboff. The free surface was modelled at 1.1D and 2.2D above the body, where D is the maximum diameter of the SUBOFF. Boundary conditions were applied as follows: a pressure inlet to simulate the forward motion of the SUBOFF, a pressure outlet to allow flow to exit without artificial reflections, and a free surface to model the interaction with the air-water interface. A symmetry plane was imposed on the longitudinal plane of the model to reduce computational effort while preserving the accuracy of the hydrodynamic simulations. Details of the domain are given in Fig. 2.

2.4 Meshing

A structured mesh was generated for both configurations using GAMBIT software, with the computational domain divided into several regions to accurately capture the complex flow characteristics around the underwater vehicle. Particular attention was given to areas with high flow gradients and vortices, such as near the vehicle's surface, sail, hydroplanes, and wake regions, where finer mesh elements were applied to enhance resolution and accurately capture detailed flow behavior. To better resolve near-wall effects, inflation layers were applied along the vehicle's surface, particularly near the leading edges and regions prone to flow separation. These layers were designed to capture velocity gradients normal to the surface with sufficient resolution while ensuring that y+ remained below the (ITTC, 2014) recommended value (<100). The maximum y+ value was 68, ensuring compatibility with the wall function approach in the k-ω SST turbulence model. The y+ distribution over the vehicle's surface is shown in Fig. 5, demonstrating the suitability of the mesh for turbulence modeling. This setup allowed for a detailed analysis of flow interactions with the vehicle, leading to accurate predictions of resistance and lift. The minimum element size on the body was 0.5 mm to maintain sufficient near-wall resolution.

2.5 Simulation Parameters

The simulations were conducted under unsteady-state conditions using the Reynolds-Averaged Navier-Stokes (URANS) equations. The *k-ω* SST turbulence model was

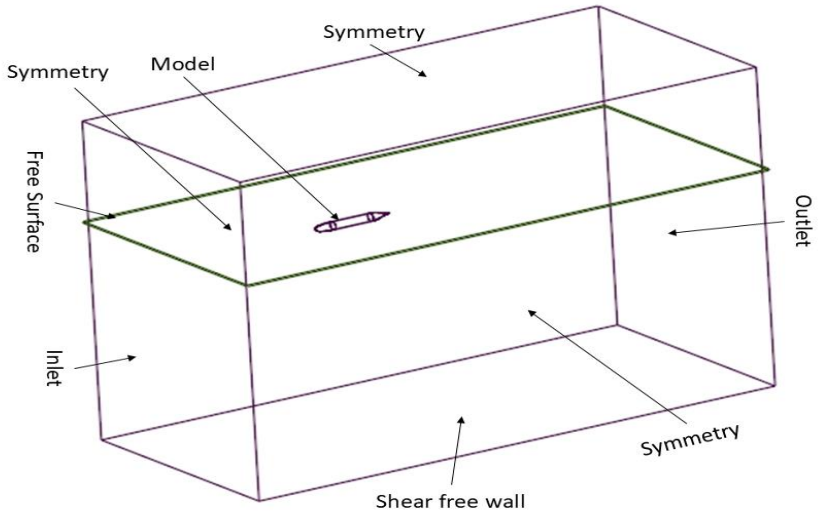

Fig. 2 Boundary conditions and computational domain

employed due to its robustness in handling adverse pressure gradients and separating flows. A time step size of 0.001 sec was selected to ensure accurate resolution of transient phenomena, following ITTC guidelines (ITTC 2014), for unsteady simulations and turbulence modeling. This choice satisfies the recommendation for resolving complex free-surface interactions and low Froude number instabilities while maintaining numerical stability. The simulations were carried out for five Froude numbers to see its impact on the hydrodynamic performance of the SUBOFF models.

2.6 Uncertainty Assessment and Grid Convergence Study

The validation of numerical results against published experimental and numerical data for the DARPA SUBOFF model is a critical step in ensuring the reliability of CFD simulations. This process involves a meticulous comparison of resistance coefficients, lift coefficients, and pressure distributions derived from CFD simulations with those obtained from experimental data. Such validation is essential as it confirms that the CFD model accurately replicates the physical phenomena observed in real-world experiments, thereby enhancing the credibility of the numerical results (Kazeminezhad et al. 2010).

A grid convergence study or GCI (Grid convergence index) is integral to the validation process, as it assesses the impact of mesh density on the results. The GCI method, recommended by the ITTC (2014) for hydrodynamic problems, serves as a robust verification procedure. The GCI method, initially proposed by Roache (1997), has been further refined by Bect et al. (2021) providing a systematic approach to quantify numerical uncertainty associated with grid spacing. This method is particularly relevant in CFD applications, where numerical uncertainty can arise from various factors, including grid spacing, time step size, and iteration count. In this study, the GCI method was employed to calculate the uncertainty of grid spacing. The refinement factor r_G in CFD is a critical parameter that influences the accuracy and efficiency of simulations and is defined as.

Table 2 Solution Setup in ANSYS Fluent

Parameters	Settings
Space	3D
Spatial discretization	Green-Gauss Node Based; second-order Upwind
Volume Fraction	Modified HRIC
Scheme	SIMPLE
Pressure	Body Force Weighted
Time Step Size	0.001 sec
Turbulence Model	*k-ω* SST
Transient Formulation	First Order Implicit

$$r_G = \frac{h_2}{h_1} = \frac{h_3}{h_2} \tag{10}$$

Where, h_1, h_2, *and* h_3 are the base sizes for coarse, medium, and fine mesh, and their values are 1m, 0.7m, and 0.5m respectively. According to the method proposed by Stovern et al. (2014), the refinement factor should exceed 1.3 to ensure that the grid resolution is sufficient to capture the essential flow features without excessive computational cost. In this study, a refinement factor of $\sqrt{2}$ has been adopted, which aligns with the recommendations of ITTC (Procedures, 2002) for achieving a balance between computational efficiency and accuracy. This choice is particularly relevant in scenarios where multiple grid configurations are tested, as it allows for systematic comparisons across different resolutions. After checking the refinement factor, the difference between the numerical results is used for calculating the grid convergence condition R_G.

$$R_G = \frac{\varepsilon_{G_{32}}}{\varepsilon_{G_{21}}} \tag{11}$$

Where,

$$\varepsilon_{G_{32}} = S_{III} - S_{II} \text{ and } \varepsilon_{G_{21}} = S_{II} - S_I$$

$\varepsilon_{G_{32}}$ indicates the change in the solutions *(S)* between grids II and III, and $\varepsilon_{G_{21}}$ is the change in the solutions

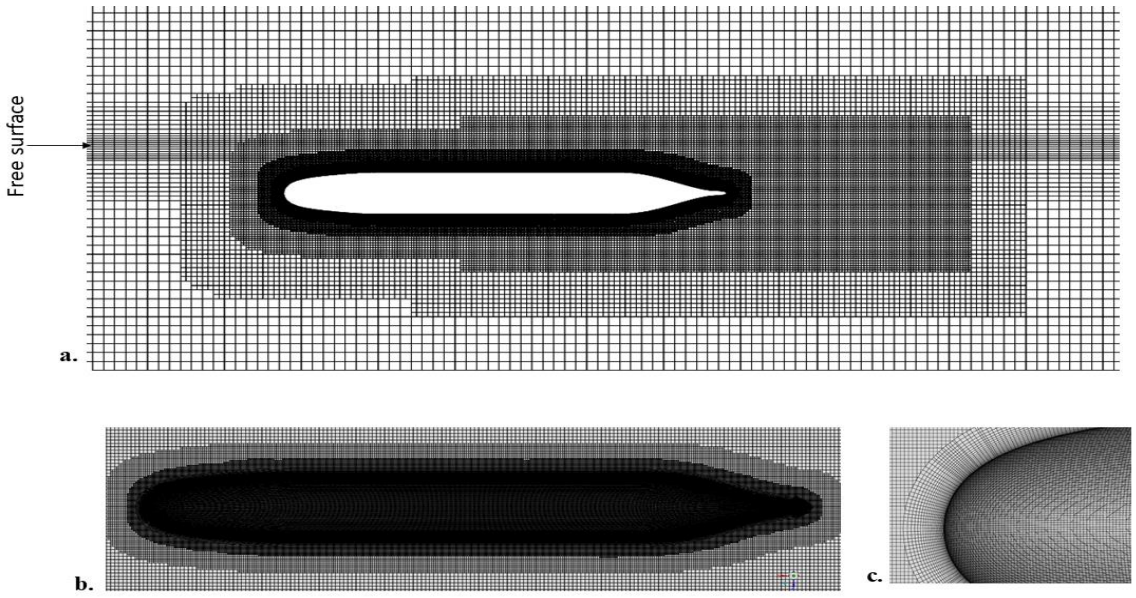

Fig. 3 Meshing around SUBOFF AFF-1, (a) Domain, (b) Near the body, (c) Inflation Layers on body

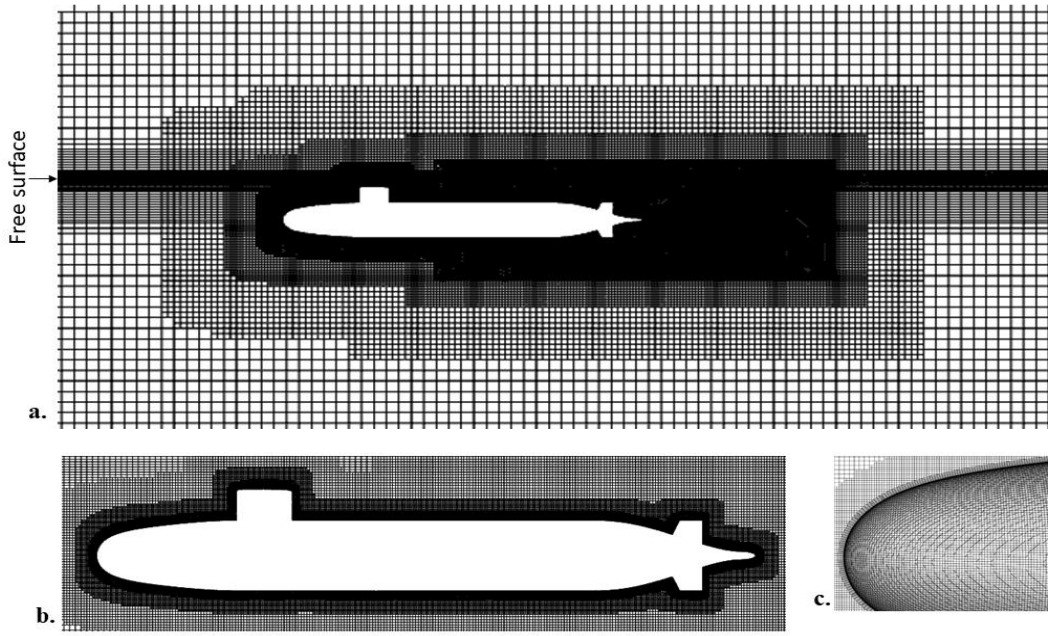

Fig. 4 Meshing around SUBOFF AFF-8 (a) overall domain, (b) near the body, (c) Inflation Layers on the body

between grids I and II. Based on the different values of RG, four conditions exist.

$0 < R_G < 1$ Monotonic Convergence

$-1 < R_G < 0$ Oscillatory Convergence

$R_G > 1$ Monotonic Divergence

$R_G < -1$ Oscillatory Divergence

If monotonic Convergence criteria are met, then the grid uncertainty U_G is determined as shown in Equation 13.

$$\boldsymbol{U_G = \frac{1}{2}|S_U - S_L|} \tag{12}$$

Where, S_L and S_U are the minimum and maximum values of the subsequent calculated results, respectively. The order of convergence for the grid, P_G is given by.

$$\boldsymbol{P_G = \frac{ln\left(\frac{1}{R_G}\right)}{ln(r_G)}} \tag{13}$$

Finally, the Grid uncertainty U_G is calculated as given in equation 14.

$$U_G = F_s \left| \frac{\varepsilon_{G32}}{S_2 r_G^{P_G} - 1} \right| \tag{14}$$

Where Fs is the safety factor, and the recommended value is 1.25. Thus, using the grids represented in Fig. 3 and Fig. 4 for bare hull and fully appended the CFD

Table 3 Total Resistance force and Lift force obtained from the simulation at 1.1D

Mesh	Elements (million)	C_T	C_L
Coarse	3.3645	0.002171	0.0008819
Medium	6.5935	0.002098	0.0008675
Fine	10.589	0.002072	0.0008612

Table 4 Calculated GCI values for normalized resistance and lift forces at 1.1D

Quantity	R_G	P_G	U_G	GCI (Fine Grid)
C_T	0.356	2.98	0.0144	0.0018
C_L	0.437	2.39	0.049	0.061

simulations are performed to estimate the resistance force in x direction acting on the SUBOFF in the fully submerged simulation, and the resistance force in the x direction, the lift force in z in the shallowly submerged simulation. Table 3 shows the normalized resistance (C_T) and lift (C_L) forces obtained from the shallowly submerged one. The normalization of the forces is carried out using the following equations.

$$C_T = \frac{F_x}{\frac{1}{2}\rho U^2 L^2} \tag{15}$$

$$C_L = \frac{F_z}{\frac{1}{2}\rho U^2 L^2} \tag{16}$$

The reduction in hydrodynamic coefficients with increasing mesh density, as shown in Table 3, indicates convergence towards a mesh-independent solution, with minimal differences between medium and fine mesh results. This suggests that further refinement may yield diminishing returns, as the fine mesh is likely close to accurately capturing the flow characteristics. Therefore, a medium or fine mesh density should be sufficient for reliable analysis of resistance and lift. Given the balance between accuracy and computational efficiency, the medium mesh emerges as an optimal choice, enhancing confidence in the predictions of the underwater vehicle's hydrodynamic performance near the free surface.

The results for GCI shown in Table 4 exhibit a consistent order of convergence, signifying enhanced accuracy as mesh refinement progresses. The low grid uncertainty (GCI) values further substantiate the robustness of these results, suggesting that the simulation approaches mesh independence, particularly within the fine grid. This convergence behavior supports confidence in the computed hydrodynamic resistance and lift forces, indicating that additional refinement would yield negligible impact on solution accuracy.

Based on the results of the GCI analysis (Table 4), the medium mesh was selected for all further simulations. The medium mesh configuration provided sufficiently low grid uncertainty (GCI) and consistent hydrodynamic

Fig. 5 Contour plot of Y+ distribution on the vehicle surface for GCI study

results compared to the fine mesh while maintaining computational efficiency.

3. RESULTS AND DISCUSSION

Results are presented for the bare hull (AFF-1) and fully appended hull (AFF-8) at three depths: 1.1D (559 mm) and 2.2D (1118 mm) from the COG to the free surface in the vertical direction, as well as deep water.

3.1. RESISTANCE FORCE

The resistance force for the DARPA Suboff model was analyzed for both (AFF-1 and AFF-8) configurations across varying Froude numbers and submergence depths. As expected, Resistance increased with speed due to intensified wave-making effects, while deeper submergence (e.g., 2.2D) reduced surface interactions, lowering resistance for both configurations. The results for the bare hull were compared with the experimental results of (Dawson, 2014) further validating the analysis.

For the bare hull (AFF-1), the resistance showed a clear dependency on depth, with a steeper reduction observed as the hull moved deeper below the free surface. This reduction is attributed to the diminished wave resistance and more streamlined flow conditions at greater depths. In contrast, the fully appended configuration (AFF-8) exhibited consistently higher resistance across all depths and speeds due to the increased wetted surface area and flow disruptions caused by the appendages. While submergence reduced resistance for AFF-8, the decrease was less pronounced compared to AFF-1, as the appendages maintained their influence on the flow dynamics.

These findings underscore the significant impact of vehicle configuration on hydrodynamic resistance. The additional resistance introduced by appendages in AFF-8 highlights the trade-off between enhanced stability and increased resistance, particularly in operations near the free surface. Figures 6 and 7 illustrate these trends, demonstrating that the fully appended configuration encounters higher resistance forces across all operational conditions, particularly at shallower depths where surface effects are more pronounced.

3.2. LIFT FORCE

The lift force for the DARPA Suboff model is evaluated for both the bare hull (AFF-1) and fully appended hull (AFF-8) configurations across varying Froude numbers and submergence depths. As

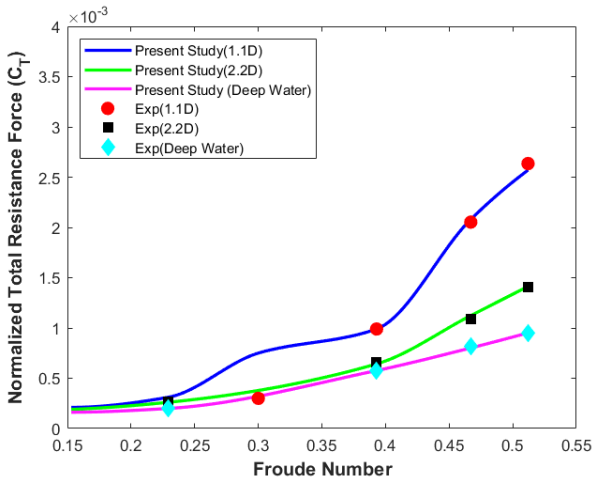

Fig. 6 Total resistance force (normalized) for SUBOFF barehull (AFF-1)

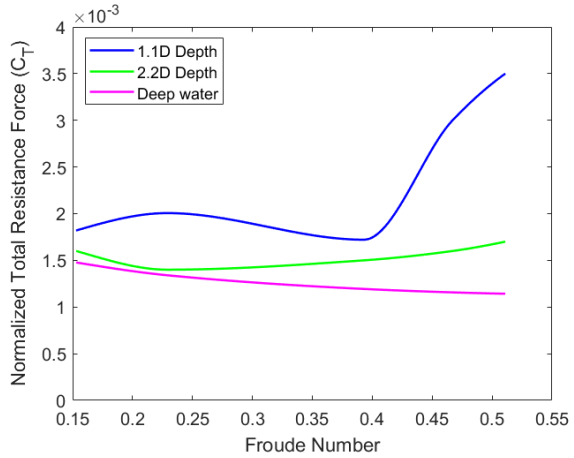

Fig. 7 Total resistance force (normalized) for fully appended hull

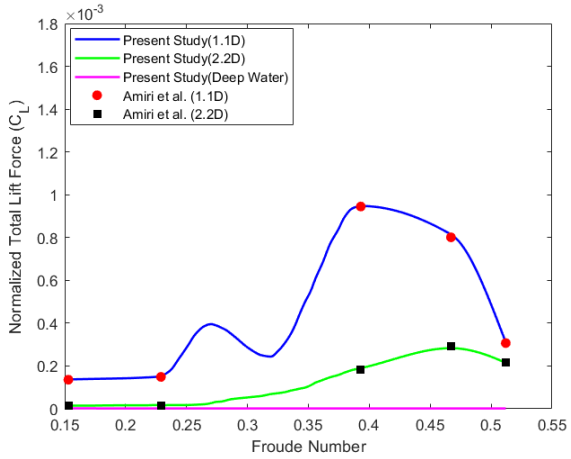

Fig. 8 Total lift force (normalized) for barehull

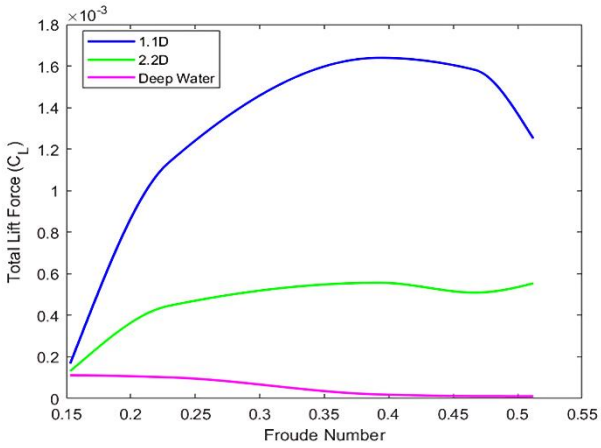

Fig. 9 Total lift force (normalized) for fully appended hull

speed increased, lift forces rose for both configurations due to the greater dynamic pressure generated around the hull at higher velocities. However, the influence of submergence depth revealed notable differences: lift forces decreased significantly as the vehicle submerged deeper, a trend consistent with reduced asymmetry in pressure distribution around the hull at greater depths. For the bare hull (AFF-1), the lift forces demonstrated a stronger dependence on depth. At shallower depths (e.g., 1.1D), interactions with the free surface created a pronounced pressure asymmetry, resulting in higher lift forces. As depth increased to 2.2D, the free surface effects diminished, leading to more symmetric pressure distribution and a marked reduction in lift. This behavior highlights the sensitivity of the bare hull's lift performance to surface proximity. Results for barehull are compared with results of (Amiri et al., 2018).

In contrast, the fully appended configuration (AFF-8) exhibited higher lift forces overall, driven by the contribution of appendages such as the sail and hydroplanes. These components increased the effective surface area, amplifying the dynamic pressure acting on the vehicle. While depth also reduced lift forces for AFF-8, the rate of reduction was less steep than for AFF-1, as the appendages maintained a significant influence on vertical force generation. The appendages not only increased lift at shallower depths but also contributed to more stable lift characteristics at varying submergence levels. Figures 8 and 9 illustrate these trends, showing that the fully appended hull generates greater lift forces than the bare hull across all operating conditions. However, the increased lift comes at the cost of additional complexity in flow dynamics, particularly at higher speeds and shallower depths. These findings emphasize the importance of considering both hull configuration and operational conditions when optimizing underwater vehicle performance near the free surface.

3.3 Free Surface Effects

The interaction between the SUBOFF model and the free surface was analyzed for AFF-1 and AFF-8 at depths of 1.1D and 2.2D across varying Froude numbers (Figs 10–13). In the VOF model, the water phase is red, the air phase is blue, and the free surface is shown in green. Conducted under calm water conditions, this study does not consider cavitation, bubble formation, or air entrainment. The gas/air phase captures free surface

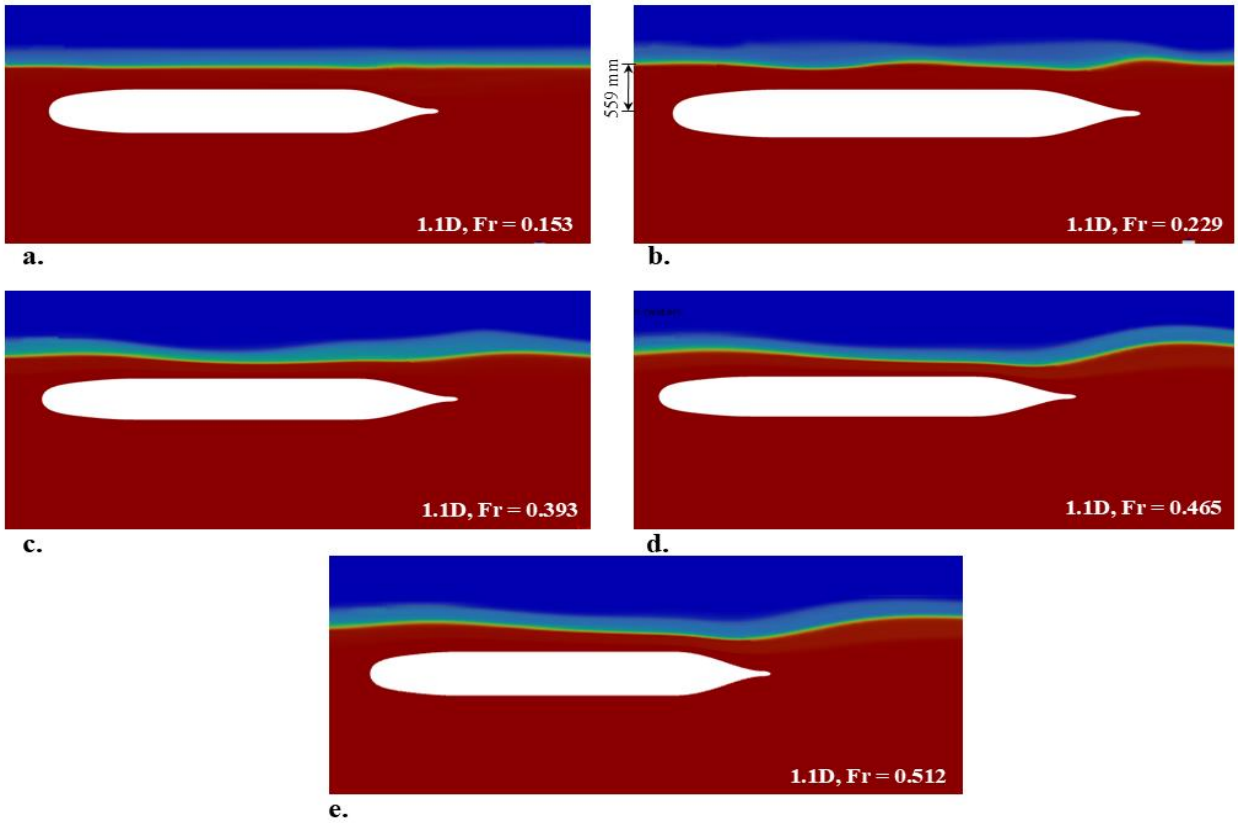

Fig. 10 Free surface effects and hydrodynamic behavior of the barehull configuration at a depth of 1.1D for Froude numbers (a) 0.153, (b) 0.229, (c) 0.393, (d) 0.465, and (e) 0.512

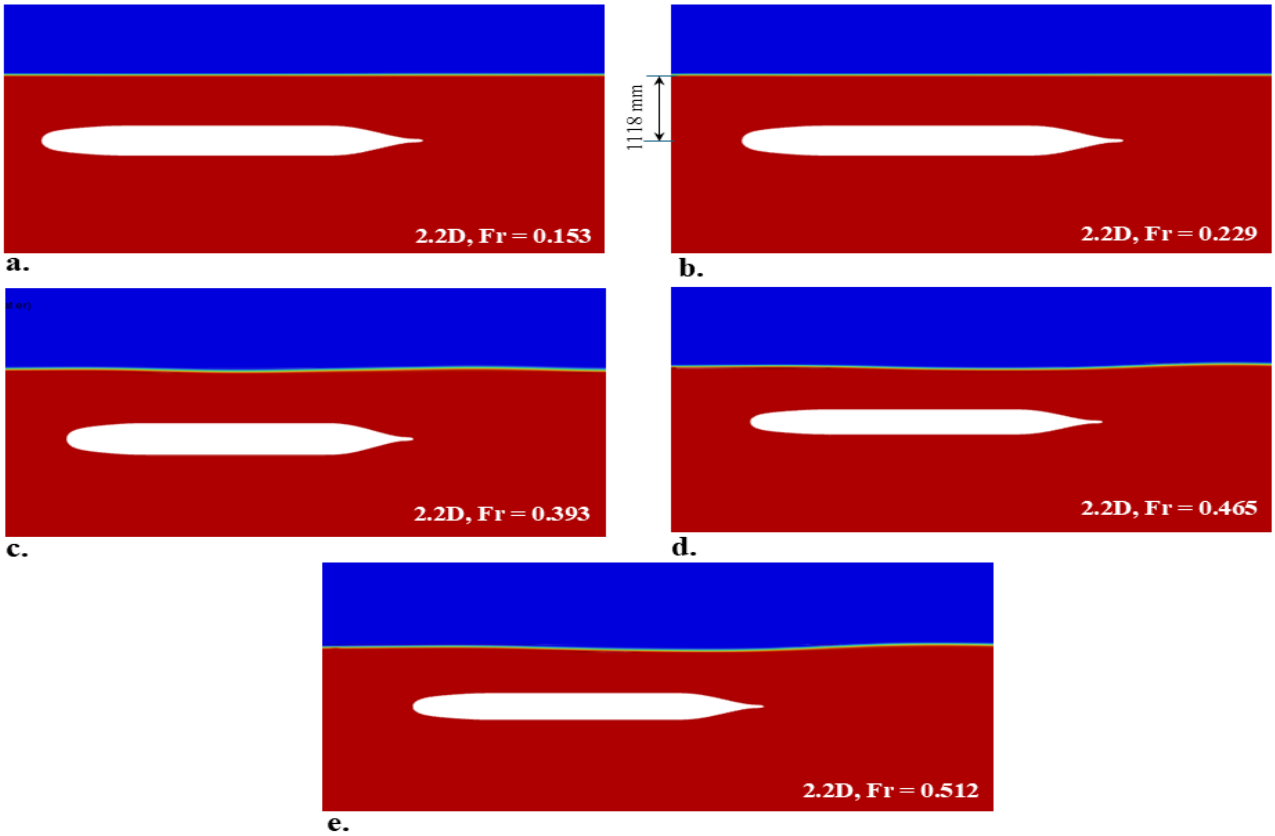

Fig. 11 Free surface effects and hydrodynamic behavior of the bare hull configuration at a depth of 2.2D for Froude numbers (a) 0.153, (b) 0.229, (c) 0.393, (d) 0.465, and (e) 0.512

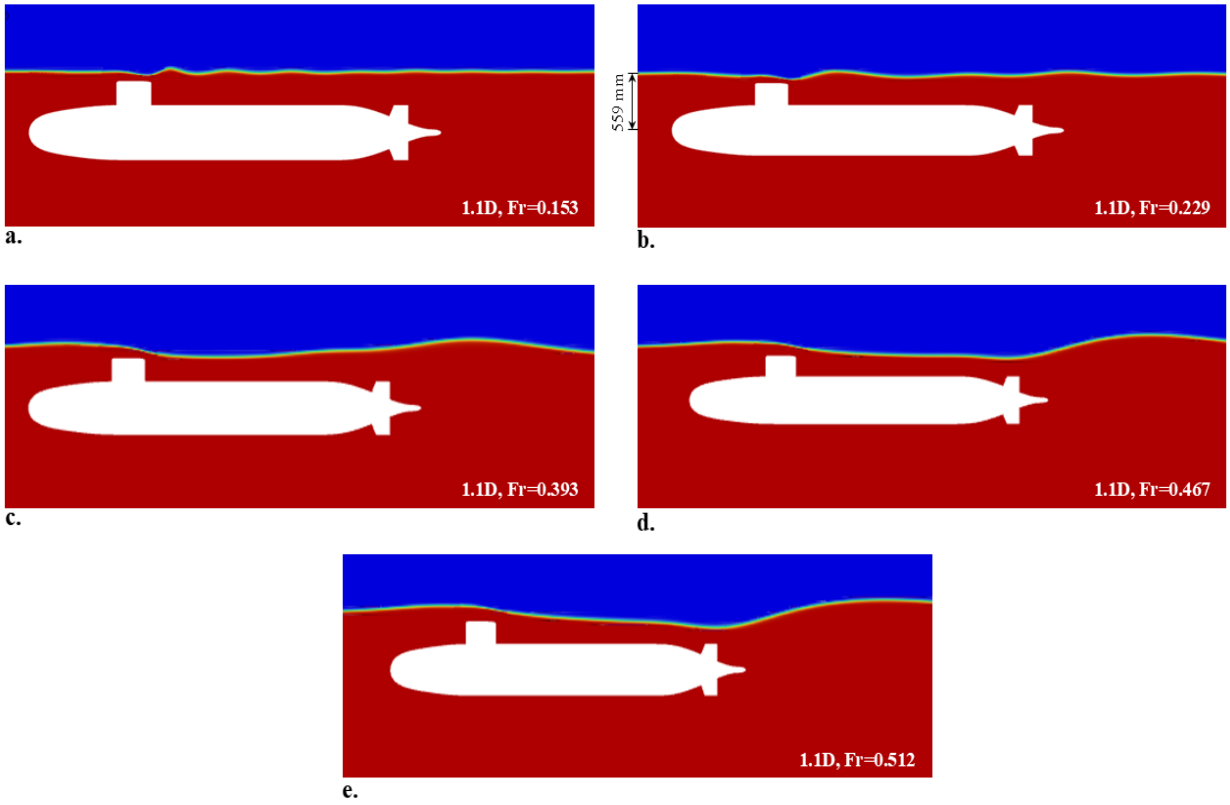

Fig. 12 Free surface effects and hydrodynamic behavior of the Fully Appended hull configuration at a depth of 1.1D for Froude numbers (a) 0.153, (b) 0.229, (c) 0.393, (d) 0.467, and (e) 0.512

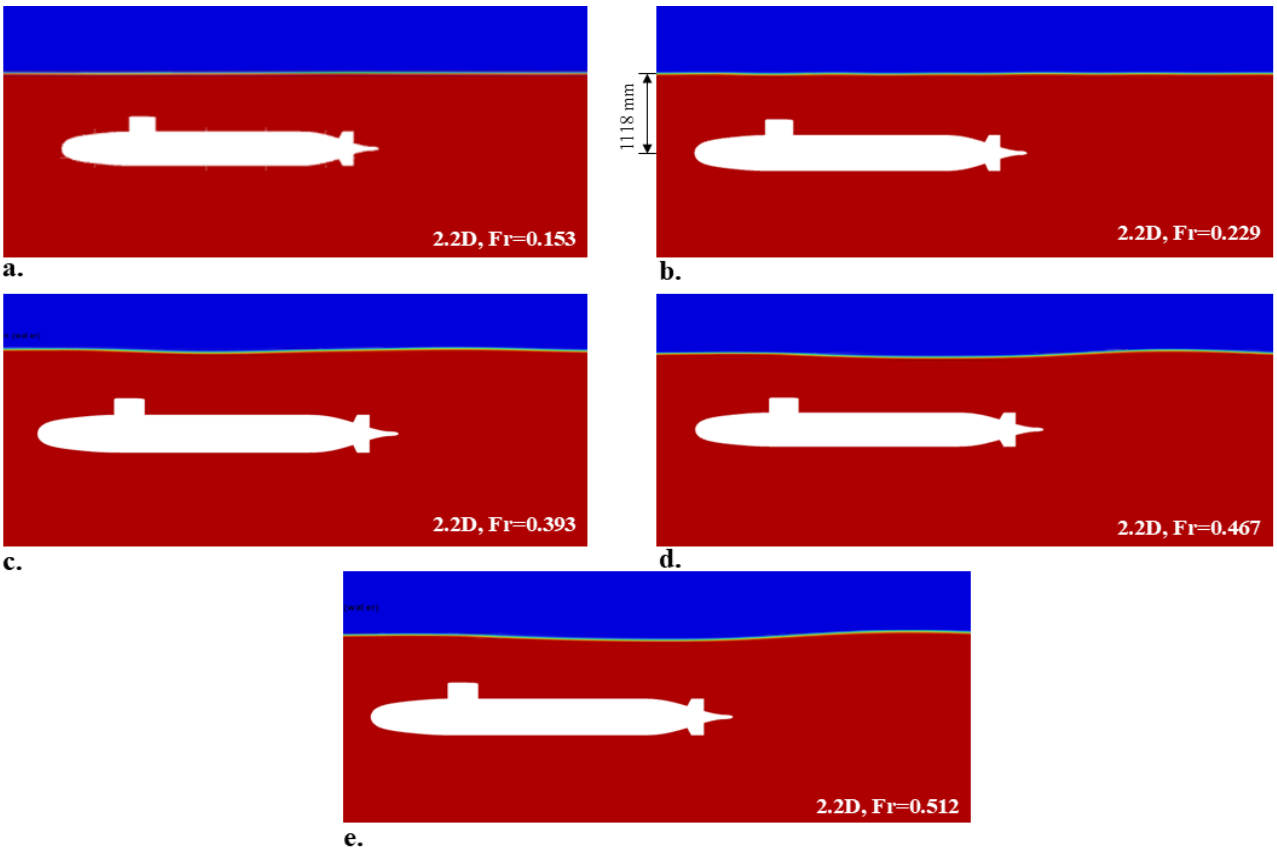

Fig. 13 Free surface effects and hydrodynamic behavior of the fully appended hull configuration at a depth of 2.2D for Froude numbers (a) 0.153, (b) 0.229, (c) 0.393, (d) 0.467, and (e) 0.512

effects, including wave generation and pressure distribution, which influence wave resistance and pressure fluctuations. The hull's interaction with the free surface produces wave patterns, wakes, and turbulence, varying with configuration and speed.

At lower Froude numbers minimal wave generation was observed for both configurations, with only small bow waves and short, stable wakes forming near the free surface. At a depth of 1.1D, the interaction was slightly more pronounced, particularly for AFF-8, where the appendages introduced localized disturbances. As the depth increased to 2.2D, these interactions diminished, resulting in narrower and less turbulent wakes.

As Froude numbers increased, the intensity of phase interactions grew significantly. At intermediate speeds (e.g., Froude 0.393), both configurations exhibited prominent bow and stern waves, with AFF-8 showing more pronounced disturbances due to the appendages. The wakes became broader and more turbulent at shallower depths, with 1.1D showing amplified asymmetry in wave patterns compared to 2.2D. The appendages in AFF-8 intensified the surface effects, causing secondary wave formations and greater wave-making resistance.

At higher speeds (e.g., Froude 0.512), the free surface interaction for both configurations was dominated by large, breaking bow waves and highly turbulent wakes. For AFF-1, these effects were primarily confined to the hull's surface, while AFF-8 experienced additional flow separations and disturbances induced by the appendages. At 1.1D, the fully appended configuration produced chaotic wave patterns, with amplified air-water interactions and spray, whereas, at 2.2D, the effects were more subdued but still significant. The breaking waves and turbulent wakes from AFF-8 highlighted the trade-off between increased stability and added hydrodynamic complexity introduced by the appendages.

It is clearly shown that the interaction intensity was consistently higher at shallower depths for both configurations, but the impact was more pronounced for AFF-8 due to the sail and stern appendages. These trends emphasize that surface proximity amplifies wave interactions, turbulence, and wake patterns. These findings underline the importance of carefully balancing vehicle configuration and operational depth to minimize adverse hydrodynamic effects while maintaining performance.

4. CONCLUSION

This study comprehensively analyzed the hydrodynamic characteristics of the DARPA SUBOFF underwater vehicle model in both bare hull (AFF-1) and fully appended hull (AFF-8) configurations, focusing on resistance and lift forces near the free surface. Using numerical simulations, it was identified that the fully appended configuration experiences notably higher resistance and lift forces than the bare hull, primarily due to the increased surface area and altered flow dynamics caused by appendages. Both configurations exhibited increasing hydrodynamic forces with speed, reflecting the significant influence of the free surface at shallower depths. These findings underscore the critical need to account for free surface effects in the design and operational planning of underwater vehicles, especially when maneuvering at varying speeds and depths. The results highlight the benefits and challenges of both hull configurations for underwater operations. While the fully appended hull demonstrated enhanced lift and stability at shallower depths, it also faced greater resistance and more complex lift behaviors, indicating a trade-off between performance and control requirements. By understanding these dynamics, this research contributes valuable insights into the optimization of hull designs and appendage configurations for different underwater applications. Future work will focus on experimental validation of the CFD results for the fully appended hull configuration using towing tank experiments. Such validation would enhance confidence in the numerical predictions, providing a more robust foundation for applying these findings in practical scenarios. Additionally, further studies incorporating environmental factors such as wave patterns along with varying submergence depths would help refine design strategies, ultimately improving the operational efficiency and stability of underwater vehicles in diverse marine applications.

ACKNOWLEDGEMENTS

The authors are thankful to the Marine Technology Center, Faculty of Mechanical Engineering, UTM, for providing the facility to conduct this research.

CONFLICT OF INTEREST

The authors declare no conflict of interest.

AUTHORS' CONTRIBUTION

Muhammad Sajjad Ahmad (Carried out the simulation work and writing of original draft). **Muhammed Amirul Asyraf Bin Hasnan** (Supervision of simulation work and review of the manuscript). **Nik Mohd Ridzuan Bin Shaharuddin** (Supervision and review of the manuscript). **Muhammad Noor Afiq Witri Muhammad Yazid** (Supervision and Review of manuscript). **Imran Shah** (Review of the manuscript, figures and tables improvement). **Muhammad Mohsin** (Review of the manuscript).

REFERENCES

Abbaszadeh, H., Daneshfaraz, R., Sume, V., & Abraham, J. (2024). Experimental investigation and application of soft computing models for predicting flow energy loss in arc-shaped constrictions. *AQUA—Water Infrastructure, Ecosystems and Society*, *73*(3), 637-661. https://doi.org/10.2166/aqua.2024.010

Abbaszadeh, H., Norouzi, R., Sume, V., Daneshfaraz, R., & Tarinejad, R. (2023a). Discharge coefficient of combined rectangular-triangular weirs using soft computing models. *Journal of Hydraulic Structures*

(JHS), *9*(1). https://doi.org/10.22055/jhs.2023.43960.1256

Abbaszadeh, H., Norouzi, R., Sume, V., Kuriqi, A., Daneshfaraz, R., & Abraham, J. (2023b). Sill role effect on the flow characteristics (experimental and regression model analytical). *Fluids*, *8*(8), 235. https://doi.org/10.3390/fluids8080235

Ahmad, M. S., Hasnan, M. A. A., Shaharuddin, N. M. R., Muhammad Yazid, M. N. A. W., Shah, I., & Bashir, N. (2024). Numerical Investigation of underwater vehicle maneuvering under static drift conditions. *CFD Letters*, *17*, 45-57. https://doi.org/10.37934/cfdl.17.5.4557

Amiri, M. M., Esperança, P. T., Vitola, M. A., & Sphaier, S. H. (2018). How does the free surface affect the hydrodynamics of a shallowly submerged submarine? *Applied Ocean Research*, *76*, 34-50. https://doi.org/10.1016/j.apor.2018.04.008

Battista, T., Valentinis, F., & Woolsey, C. (2023). A Maneuvering Model for an underwater vehicle near a free surface—Part II: Incorporation of the free-surface memory. *IEEE Journal of Oceanic Engineering*, *48*(3), 740–751. https://doi.org/10.1109/JOE.2022.3229919

Bect, J., Zio, S., Perrin, G., Cannamela, C., & Vazquez, E. (2021). On the quantification of discretization uncertainty: comparison of two paradigms. arXiv preprint arXiv:2103.14559.

Chen, Y., Huang, C., Yan, W., He, G., & Zhang, S. (2024). Numerical Study on the sloshing behaviors of dual liquid tanks with gas inflow. *Journal of Applied Fluid Mechanics*, *17*(9), 1885-1895. https://doi.org/10.47176/jafm.17.9.2595

Daneshfaraz, R., Rezaie, M., Aminvash, E., Süme, V., Abraham, J., & Ghaderi, A. (2023). On the effect of green nonstructural materials on scour reduction downstream of grid dissipators. *AQUA—Water Infrastructure, Ecosystems and Society*, *72*(7), 1344-1357. https://doi.org/10.2166/aqua.2023.108

Dawson, E. (2014). *An investigation into the effects of submergence depth, speed and hull length-to-diameter ratio on the near surface operation of conventional submarines* [PhD Thesis, University of Tasmania]. Google Scholar.

F-Pedrera Balsells, M., Grifoll, M., Espino, M., Cerralbo, P., & Sánchez-Arcilla, A. (2020). Wind-driven hydrodynamics in the shallow, micro-tidal estuary at the fangar bay (Ebro Delta, NW Mediterranean Sea). *Applied Sciences*, *10*(19), 6952. https://doi.org/10.3390/app10196952

Gabriel, S. A., Cameron, A., Fowler, A., & Pook, D. A. (2020, 2020-12-11). *Modelling Hydrodynamic loads for manoeuvring simulations of underwater vehicles.* 22nd Australasian Fluid Mechanics Conference AFMC2020,

Ilyas, M., Aziz, S., Shah, I., Khan, A., & Jung, D. W. (2023). Experimental stability analysis of vertical takeoff and landing system based on robust control strategy. *Applied Sciences*, *13*(20), 11209. https://www.mdpi.com/2076-3417/13/20/11209

ITTC (2014). Practical Guidelines for Ship CFD Applications, 20 . https://www.ittc.info/media/8165/75-03-02-03.pdf

Jiawei, G., Chuan, L., Shifeng, Y., Zhiyuan, C., & Jibo, C. (2023). Structural Design and hydrodynamic coefficient calculation of observation-class ROVs. *Journal of Engineering Research and Reports*, *25*(3), 104-113. https://doi.org/10.9734/jerr/2023/v25i3895

Kazeminezhad, M., Yeganeh-Bakhtiary, A., & Etemad-Shahidi, A. (2010). Numerical investigation of boundary layer effects on vortex shedding frequency and forces acting upon marine pipeline. *Applied Ocean Research,* *32*(4), 460-470. https://doi.org/10.1016/j.apor.2010.10.002

Lambert, W., Miller, L., Brizzolara, S., & Woolsey, C. (2023). A free surface corrected lumped parameter model for near-surface horizontal maneuvers of underwater vehicles in waves. *Ocean Engineering*, *278*, 114364. https://doi.org/10.1016/j.oceaneng.2023.114364

Ling, X., Leong, Z. Q., Chin, C. K., & Woodward, M. (2022). Free surface effect on the hydrodynamics of an underwater vehicle hullform, The DARPA SUBOFF. *International Journal of Maritime Engineering*, *164*(A1). https://doi.org/10.5750/ijme.v164i1.732

Luo, S., Guan, X., & Wang, X. (2023, May). Hydrodynamic coefficient estimation for underwater vehicle maneuvering. In International Conference on Computer, Artificial Intelligence, and Control Engineering (CAICE 2023) (Vol. 12645, pp. 17-23). SPIE. https://doi.org/ 10.1117/12.2680829

Meng, Q., Zhou, F., Ma, X., Xuan, J., Zhang, H., Wang, S., Ni, X., Zhang, W., Wang, B., Li, D., Tian, D., Li, J., Zeng, J., Chen, J., & Huang, D. (2022). Response Process of coastal hypoxia to a passing typhoon in the east China sea. *Frontiers in Marine Science*, *9*. https://doi.org/10.3389/fmars.2022.892797

Menter, F. R. (1994). Two-equation eddy-viscosity turbulence models for engineering applications. *AIAA journal*, *32*(8), 1598-1605. https://doi.org/10.2514/3.12149

Mitra, A., Panda, J. P., & Warrior, H. V. (2019). The effects of free stream turbulence on the hydrodynamic characteristics of an AUV hull form. *Ocean Engineering*, *174*, 148–158. https://doi.org/10.1016/j.oceaneng.2019.01.039

Mitra, A., Panda, J. P., & Warrior, H. V. (2020). Experimental and numerical investigation of the hydrodynamic characteristics of autonomous underwater vehicles over sea-beds with complex topography. *Ocean Engineering*, *198*, 106978. https://doi.org/10.1016/j.oceaneng.2020.106978

Procedures, I. (2002). U*ncertainty analysis in CFD, uncertainty assessment methodology and Procedures.* Proceedings of the International Towing Tank Conference, Venice, Italy,

Roache, P. J. (1997). Quantification of uncertainty in computational fluid dynamics. *Annual review of fluid Mechanics, 29*(1), 123-160.

Roddy, R. F. (1990). *Investigation of the stability and control characteristics of several configurations of the DARPA SUBOFF model (DTRC Model 5470) from captive-model experiments.* David Taylor Research Center, Ship Hydromechanics Department, DTRC/SHD-1298-08.

Stovern, M., Felix, O., Csavina, J., Rine, K. P., Russell, M. R., Jones, R. M., ... & Sáez, A. E. (2014). Simulation of windblown dust transport from a mine tailings impoundment using a computational fluid dynamics model. *Aeolian research, 14*, 75-83.

Valentinis, F., Battista, T., & Woolsey, C. (2023). A maneuvering model for an underwater vehicle near a free surface—Part III: Simulation and control under waves. *IEEE Journal of Oceanic Engineering*, *48*(3), 752-777. https://doi.org/10.1109/JOE.2023.3234811

Walker, K. L., Gabl, R., Aracri, S., Cao, Y., Stokes, A. A., Kiprakis, A., & Giorgio-Serchi, F. (2021). Experimental validation of wave induced disturbances for predictive station keeping of a remotely operated vehicle. *IEEE Robotics and Automation Letters*, *6*(3), 5421-5428. https://doi.org/10.1109/LRA.2021.3075662

Xu, P., Chen, J., Guo, Y., & Luo, W. (2024a). Comparative Study on hydrodynamic characteristics of under-water vehicles near free surface and near ice surface. *Journal of Marine Science and Engineering*, *12*(12), 2131. https://doi.org/10.3390/jmse12122131

Xu, Y., Shi, W., Song, Y., & Hou, H. (2024b). Hydrodynamics of a Remora-inspired autonomous underwater vehicle approaching and docking to a benchmark submarine. *Ocean Engineering*, *291*, 116447. https://doi.org/10.1016/j.oceaneng.2023.116447

Zhang, D., Zhao, B., & Sun, J. (2024). Hydrodynamic performance and wake study of an UUV sailing near the free surface. *Frontiers in Marine Science*, *11*. https://doi.org/10.3389/fmars.2024.1416166